Thermoelectric power generation in the core of a nuclear reactor

Nicholas Kempf [a,1], Mortaza Saeidi-Javash [a,1], Haowei Xu [b,1], Sheng Cheng [c,d], Megha Dubey [c,d], Yaqiao Wu [c,d], Joshua Daw [e], Ju Li [b,2], Yanliang Zhang [a,*,2]

[a] Department of Aerospace and Mechanical Engineering, University of Notre Dame, Notre Dame, IN 46556, USA
[b] Department of Nuclear Science and Engineering, Massachusetts Institute of Technology, Cambridge, MA 02139, USA
[c] Micron School of Materials Science and Engineering, Boise State University, Boise, ID 83725 USA
[d] Microscopy and Characterization Suite, Center for Advanced Energy Studies, Idaho Falls, ID 83401 USA
[e] Measurement Sciences Laboratory, Idaho National Laboratory, Idaho Falls, ID 83415, USA

ABSTRACT

Thermoelectric energy converters offer a promising solution to generate electrical power using heat in the nuclear reactor core. Despite significant improvements in thermoelectric efficiency of nanostructured materials, the performance of these advanced materials has yet to be demonstrated in the harsh radiation environment of a reactor core. Herein, we demonstrate a thermoelectric generator (TEG) made from nanostructured bulk half-Heusler (HH) materials generating stable electrical power density > 1140 W/m^2 after 30 days in the MIT Nuclear Research Reactor under an unprecedented fast-neutron (>1 MeV) fluence of 1.5×10^{20} n/cm^2. Despite an initial degradation due to irradiation damage when operating under relatively low temperatures, our TEG showed a 20-fold increase in power output when operating under high temperature due to in-situ annealing and resulting thermoelectric property recovery. First-principles modeling indicates that a chemically disordered metallic phase was formed under irradiation at lower temperatures, resulting in a drastic degradation in thermoelectric properties, while at sufficiently high temperatures the system returned to the initial chemically ordered HH phase and the thermoelectric properties recovered. Transmission electron microscopy and electron diffraction demonstrated that the chemically disordered phase was formed upon ion irradiation, confirming the prediction from first-principles simulations. The results suggest that with proper control over the TEG operating temperatures, the nanostructured bulk TEGs could produce stable electrical power and operate indefinitely in the core of a nuclear reactor.

1. Introduction

Nuclear reactors are among the energy sources that will continue to be implemented as the world tends toward carbon–neutral electricity production [1,2]. The safety of nuclear power plants can be increased by monitoring critical nuclear fuel parameters like fuel thermal conductivity and temperature. However, such monitoring requires sensors, which in turn require electrical power. Herein we demonstrate the application of a state-of-the-art thermoelectric generator (TEG) as an energy scavenging device that may be used to power sensors and instrumentation in the core of a nuclear reactor, thereby increasing power plant safety without the need for costly data and power cables. Solid-state TEGs are highly scalable energy converters of heat into electrical power through the Seebeck effect [3,4]. While most current thermoelectric research focuses on increasing material performance [5–13], there are relatively few studies on applications of thermoelectric materials and devices in extreme environments. Nuclear fission reactors provide heat flux rich conditions that can be harvested to power primary

loop sensors, instrumentation, and other critical equipment during both normal operations as well as during an extended loss of power condition, such as a station blackout event [14]. Radioisotope heated TEGs are already used in deep space exploration where there is insufficient solar irradiance [15], and could also be used in nuclear waste monitoring using the heat generated during long-term decay. While there have been some studies of the irradiation effect on thermoelectric performance of bulk thermoelectric materials like germanium telluride, silicon–germanium, etc. [16–18], they were typically exposed to neutron fluences between 10^{13} to 10^{18} n/cm^2 [15,19]. The combination of thermal and fast neutron irradiation at relatively low temperature (<200 °C) created point defects in these materials, reducing carrier mobility and lowering thermoelectric performance. There are no reports on the in-situ power generation and performance of thermoelectric materials in the core of a nuclear reactor while under extreme radiation exposure.

Thermoelectric material performance is determined by the thermoelectric figure of merit $ZT = \alpha^2 \sigma T / (\kappa_e + \kappa_l)$, where α is the Seebeck coefficient, σ is the electrical conductivity, T is the absolute temperature,

---

Nomenclature

Abbreviations

TEG	thermoelectric generator
HH	half-Heusler
dpa	displacements per atom
SThM	scanning thermal microscopy
TEM	transmission electron microscopy
SAED	selected area electron diffraction

Greek letters

α	Seebeck coefficient (V/K)
σ	electrical conductivity (S/m)
κ	thermal conductivity (W/m•K)

Symbols

T	absolute temperature (K)
ZT	thermoelectric figure of merit (dimensionless)

Subscripts

e	electronic component (of thermal conductivity)
l	lattice component (of thermal conductivity)
h	hot side
c	cold side

and κ_e and κ_l are the electronic and lattice components of thermal conductivity, respectively. Nanostructured bulk half-Heusler (HH) alloys are promising thermoelectric materials for nuclear energy applications due to their thermal stability, mechanical strength, and significantly increased ZT compared to their bulk counterparts [12,13,20–23]. The structure of HH alloys consists of 4 face-centered cubic sublattices with the formula $A_1B_1C_1D_0$, where A=(0,0,0), B=(1/4, 1/4, 1/4) are occupied by transition metals, C=(½, ½, ½) is occupied by main group element, and D=(¾, ¾, ¾) ideally should remain vacant. Nanostructured materials may have improved radiation tolerance due to a high density of nanostructures and grain boundaries that can act as sinks for irradiation induced defects [20,21,24–32]. Using current state-of-the-art nanostructured thermoelectric materials, our TEG produced electrical power within a 6 MW nuclear research reactor with a core power density of about 70 kW per liter and fast neutron flux of 1.3×10^{14} n/cm^2/s (>0.1 MeV) and 6.1×10^{13} n/cm^2/s (>1 MeV). It was found that the TEG performance can be significantly compromised in the core of a

reactor due to irradiation-induced damage if the TEG operates at sufficiently low temperatures; however, the TEG power output increased by a factor of 20 within a matter of hours after the TEG average operating temperature was increased by just 30%, from 226 °C to 373 °C. Meanwhile, TEG power output steadily increased for the remainder of the 30-day in-core test while the reactor operated at full power. These results suggest that thermally activated in-situ healing of irradiation damage has occurred, allowing the TEG to provide a stable source of electrical power even in the extreme environment of a reactor core.

The TEG is comprised of 28 pairs of nanostructured bulk n-type $Hf_{0.25}Zr_{0.75}NiSn_{0.99}Sb_{0.01}$ and p-type $Nb_{0.75}Ti_{0.25}FeSb$ half-Heusler materials referred to as HHN and HHP, respectively, each with peak ZT near 1.0 at 600 °C [21,22]. The performance of similar nanostructured bulk HH materials has been demonstrated in an automotive TEG that produced over 1 kW of electrical power from the exhaust waste heat of an internal combustion engine [33,34] as well as in a residential micro combined heat and power system [35]. Our HH TEG was inserted into the core of a research reactor at the Massachusetts Institute of Technology (MIT) nuclear reactor laboratory. The core of the MIT reactor is shown in Fig. 1, along with a photograph of the TEG that was inserted into the reactor.

As shown in Fig. 1, the abundant radiation and coolant flow available in the nuclear reactor makes the TEG an ideal power harvesting technology for in-core applications. A test capsule (Supplementary Fig. S1 and Fig. S2) was designed and constructed to house the TEGs, a tungsten susceptor, measurement wire connections, and thermocouples. The tungsten susceptor provides heating to the TEG hot side using thermal excitation by gamma rays while the cooling water running in the reactor provides the heat sink for the TEG cold side. The TEG electrical resistance, open circuit voltage, and power output as a function of electrical current were measured continuously during the in-core test using a custom in-house-constructed testing system. Additional details about the in-core measurement can be found in the Methods Section and in Supplementary Information.

2. Results and discussion

2.1. In-core thermoelectric generator performance

In-situ performance of the TEG in the reactor core was continuously measured for 30 days. Fig. 2a shows the TEG peak power and the TEG hot- and cold-side temperatures for the duration of the in-core test, while Fig. 2b shows the TEG electrical resistance and the effective Seebeck coefficient, which is defined as the TEG open circuit voltage upon the
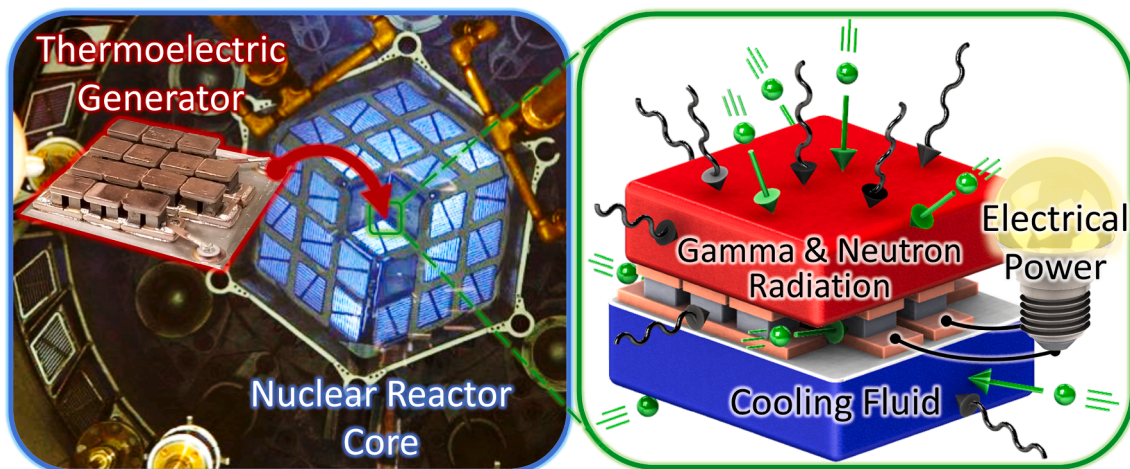

Fig. 1. Photograph of the core of the nuclear reactor at the MIT nuclear reactor laboratory (left) with inset showing a photograph of the nanostructured half-Heusler TEG, and schematic showing a TEG producing electrical power from heat supplied by a gamma susceptor on the TEG hot side and cooling fluid cooling the TEG cold side (right).
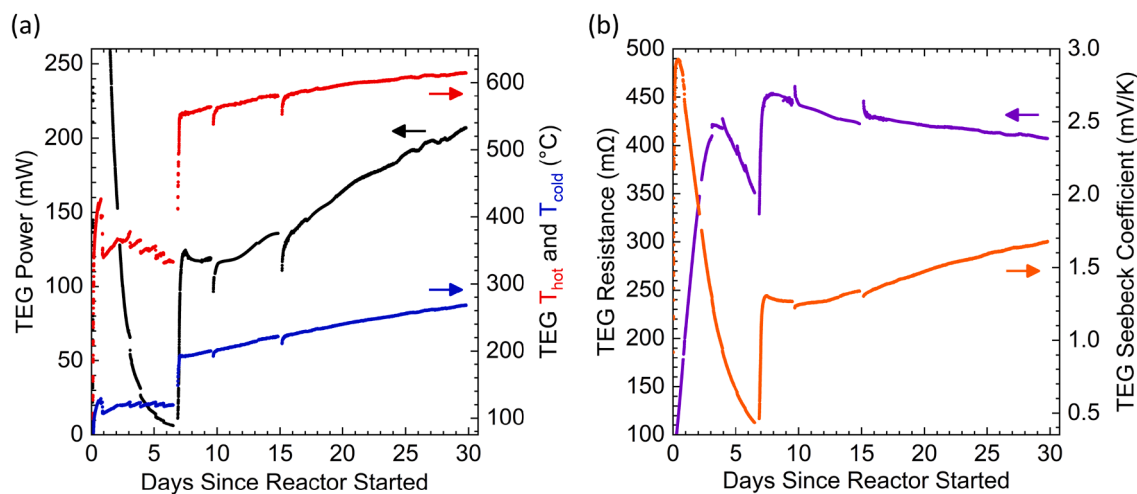
Fig. 2. TEG in-core performance and measurement results: (a) TEG peak power (black) along with TEG hot-side temperature T_{hot} (red) and cold-side temperature T_{cold} (blue); (b) TEG resistance (violet) and TEG effective Seebeck coefficient (orange).

temperature difference across the TEG.

The reactor initially ramped to full power (5.7 MW) and the TEG power output quickly reached a maximum value of 1.5 W while the TEG hot-side and cold-side temperatures were 378 °C and 110 °C, respectively (to clearly show the change in power for the duration of the experiment, some transient data during the first 2 days, including the peak to 1.5 W, is omitted from Fig. 2a). Over the following 6 days of in-core testing, the reactor power was intermittently lowered to 3.2 MW, resulting in the 5 drops in TEG hot-side temperature shown in Fig. 2a. During this period, the TEG was operating at relatively low temperatures and the TEG output power experienced a severe drop to 6 mW due to a significant decrease in Seebeck coefficient while electrical resistance sharply increased. This increase in TEG electrical resistance is attributed to the accumulation of irradiation-induced defects that act as scattering centers for charge carriers, lowering carrier mobility and thus electrical conductivity. It is expected that these defects also act to scatter phonons, reducing thermal conductivity. This is supported by Scanning Thermal Microscopy [36] (SThM) which will be discussed in a later section. The reactor was brought back to full power on day 7 and remained at 5.7 MW for the remainder of the test with the exception of two temporary shutdowns for maintenance on days 10 and 15 (some of the transient data from these shutdowns and startups are omitted from Fig. 2). The increase in reactor power on day 7 resulted in a rapid yet slight increase in the TEG hot- and cold-side temperatures from 333 °C and 120 °C to approximately 555 °C and 192 °C, respectively. Within a matter of hours, the TEG open-circuit voltage increased by over 400% despite relatively modest increases of 30% and 70% in mean TEG temperature and the temperature difference across the TEG, respectively (in these temperature ranges, the open-circuit voltage is approximately proportional to the temperature difference for a TEG operating in normal conditions outside of a nuclear reactor core). Even though TEG resistance increased 28% during this transient period, the TEG peak power output showed a 1,926% increase compared to the power output on day 6.5 just before the reactor went to high power. Such a dramatic revival of TEG performance indicates in-situ healing of irradiation induced damage, and the detailed mechanisms will be presented in the following sections which discuss post irradiation examinations and theoretical modeling to explain the changes in thermoelectric material properties.

3. Ion irradiation and post-irradiation examination

To simulate neutron irradiation damage without rendering the thermoelectric materials radioactive, the n- and p-type half-Heusler materials were irradiated with 4.5 MeV alpha particles from an ion beam accelerator. In preparation for irradiation, the bars were polished and copper shields were used to block alpha particles in selected regions of the bar (Supplementary Fig. S3). Each bar had sections separated by shields and each region was irradiated to a dose of 0.005, 0.05, or 0.5 displacements per atom (dpa). After irradiation, the copper shields were removed and SThM [36] was used to simultaneously measure the Seebeck coefficient and thermal conductivity of irradiated and non-irradiated regions at the same time, eliminating uncertainties introduced by measuring the samples at different times, such as oxidation and contamination. The SThM results of the selectively irradiated sample, shown in Fig. 3, indicate an exponential decay in Seebeck coefficient with increasing irradiation dose beyond 0.005 dpa in both the n- and p-type materials. Upon ion irradiation to a dose of 0.05 dpa, the Seebeck coefficients of the n- and p-type materials decreased by 46% and 59%, respectively. At 0.5 dpa, Seebeck coefficient fell by 91% and 99%, respectively. On the other hand, at 0.05 dpa there was a sharp reduction of 61% and 48% in thermal conductivity, respectively, but a partial recovery corresponding to reductions of only 48% and 40% at 0.5 dpa. The reductions in thermal conductivity at the low and intermediate doses are attributed to irradiation-induced defects (Fig. 4 and Supplementary Fig. S4 for HHN and HHP, respectively) that act as phonon scattering centers, while the increase in conductivity at the highest dose is expected to be due to an increase in the electronic component of thermal conduction that outweighs the reduction in conductivity due to defect scattering, as would be expected after the phase change to the disordered metallic phase (see the Phase Change Mechanism section). Additional details about the SThM measurement can be found in the Supplementary Materials.

To uncover the irradiation-induced compositional and microstructural changes, Transmission Electron Microscopy (TEM) and Selected Area Electron Diffraction (SAED) were performed on the irradiated and non-irradiated HHN and HHP samples. The TEM images in Fig. 4a-c and Supplementary Fig. S4a-c show a significant difference in grain sizes between the non-irradiated and irradiated regions of HHN and HHP, respectively. These indicate that ion irradiation provided the kinetic facilitation for grain coarsening to occur in both materials. The original HHN and HHP were synthesized and sintered from solid powders, with a wide distribution of initial grain sizes. After radiation to 0.5 dpa, many of the smallest grains have disappeared while the larger grains grew somewhat. Furthermore, in HHN sub-10 nm radiation defects (dislocation loops and voids) appeared between 0.05 and 0.5 dpa, decreasing the crystallinity of the sample.

Also shown in Fig. 4a-c and Supplementary Fig. S4a-c is a difference in the apparent crystallinity and/or defect density among the regions,
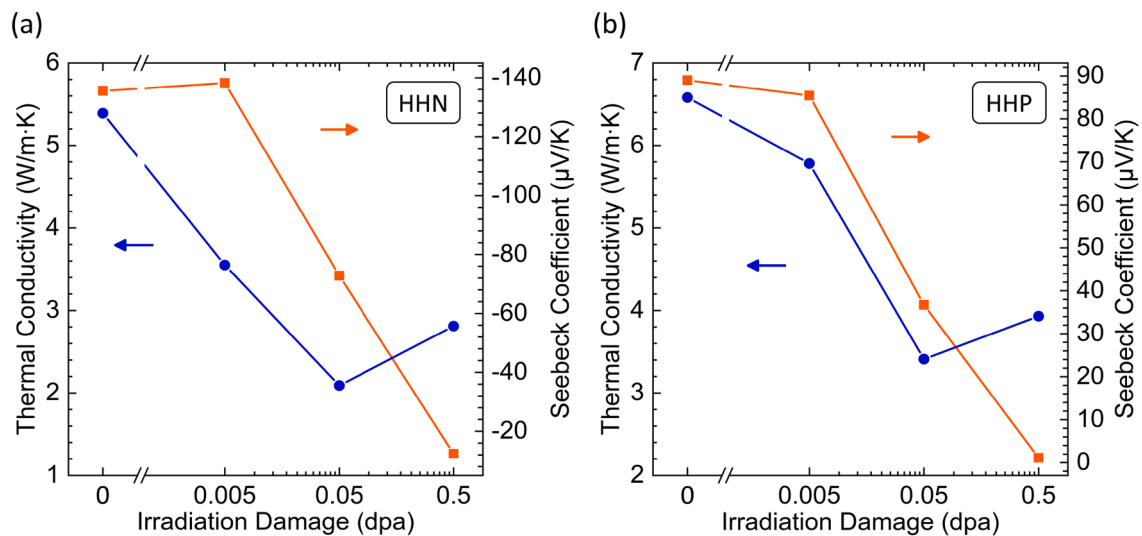
Fig. 3. SThM results showing thermal conductivity and Seebeck coefficient of the ion-irradiated (a) HHN and (b) HHP materials.

which is highlighted further at increased magnification (Fig. 4d-f,i and Supplementary Fig. S4d-f). In the case of the n-type material, the non-irradiated specimen in Fig. 4a,d shows a relatively high density of nanoscale precipitates within a matrix of highly crystalline grains when compared to the specimen irradiated to 0.05 dpa shown in Fig. 4b,e. The precipitates are attributed to the presence of Zirconium and Hafnium-rich secondary phases. As shown in Fig. 4c,f,i the density of these precipitates is lower in the 0.5 dpa sample, which indicates irradiation induced dissolution of these pre-existing Zirconium and Hafnium-rich secondary phases. However, the specimen irradiated to 0.5 dpa also has a very high density of other nanoscale defects, which are a uniform distribution of nanoscale cluster defects such as dislocation loops, which are also seen in the p-type material (Supplementary Fig. S4c,f). Some voids can also be seen in e.g. Fig. 4c and Fig. S4c. Additionally, the insets in Fig. 4d-f show that with increasing irradiation dose, the family of planes of the form $\langle 2n-1, 2n-1, 2m-1 \rangle$, where $n, m = 1, 2, \cdots$, has diminishing spot intensity compared to all other planes. This result confirms that the irradiation induced a phase change in the n-type material from the native semiconducting half-Heusler phase $A_1B_1C_1D_0$ to a metallic phase of the form $A_1B_{1-x}C_1D_x$, as described in the following section and in Supplementary Fig. S5. The same change is observed in the SAED patterns of the p-type material (Supplementary Fig. S4d,e), but to a lesser extent. Note that SAED patterns could not be obtained for the HHP sample irradiated to 0.5 dpa because the sample became amorphous upon thinning in preparation for TEM.

4. Phase change mechanism

As described above, the TEG electrical power output dropped significantly during the first week while the reactor was kept at low power and TEG temperatures were relatively low. The TEG power recovered rapidly when the reactor was brought to full power and the temperature increased on day 7. The drastic recovery of the TEG performance indicates atomic level phase change. The forthcoming discussion considers n-type $Hf_{0.25}Zr_{0.75}NiSn$ only; however, the same phenomema are predicted for the p-type material $Nb_{0.75}Ti_{0.25}FeSb$ and the analogous calculations and figures can be found in the Supplementary Information (Supplementary Fig. S6). The dopant $Sb_{0.01}$ is not included in the simulations due to the limited computational power. The atomic structure of $Hf_{0.25}Zr_{0.75}NiSn$ is shown in the inset of Fig. 5a.

The sites occupied by Zr (Hf), Ni, and Sn are labeled as A, B, and C, respectively. There are also vacancy sites between A and C sites, which are called D sites. When all Ni atoms occupy B sites, one has the pristine

half-Heusler structure. Ab initio calculations reveal the system is semiconducting (Fig. 5b) and the Seebeck coefficient is on the order of $100\mu V/K$, which agrees with experimental results ($135 \sim 142\mu V/K$ at the measured carrier concentration of $2.65 \times 10^{20} cm^{-3}$ in the case of the n-type material). Under irradiation, the atoms are knocked around and some of the sites which are normally vacant (D sites) become occupied. One may expect that Zr (Hf)/Ni/Sn atoms would randomly occupy A/B/C/D sites. On the other hand, calculations indicate that such an entirely random structure is highly energetically unstable, and the resulting material would spontaneously become structurally disordered (amorphous). This contrasts with the SAED patterns which indicate a crystalline structure that is only partially chemically disordered. After careful examination, we found that if some Ni atoms move from B to D sites while Zr (Hf)/Sn atoms stay on the A/C sites, the structure is stable at sufficiently low temperature and will remain crystalline. Remarkably, the thermoelectric properties of the system change dramatically when some Ni atoms move from B to D sites ($A_1B_{1-x}C_1D_x$ occupation). A 12-atom $Hf_1Zr_3Ni_4Sn_4$ supercell was used with one Ni atom on the D site ($x = 0.25$). In this case, the system becomes metallic (Fig. 5b). The Seebeck coefficient is reduced to the order of $10\mu V/K$, smaller by a factor of 10 compared to the native structure when all Ni atoms are on the B sites. This explains the sharp drop in Seebeck coefficient and thermoelectric voltage of the TEG when the reactor is first operating at relatively low power during the first week. As the temperature rose on day 7, the system quickly annealed and the increased temperature provided the activation energy necessary for Ni atoms to jump back to their original B sites, which is energetically favorable (Fig. 5a). Nudged Elastic Band (NEB) calculations [37] indicate that the energy barrier for Ni atoms to jump back from D to B sites is about 1.75 eV (Fig. 5a). From transition state theory, the transition rate for each nickel atom from D to B is about 0.01 s^{-1} at 600 K, which is sufficiently fast considering the experimental timescale is on the order of hours/days.

Based on the mechanism proposed above, Ni atoms jumped from B to D sites during the first week and the system became increasingly metallic; however, the TEG electrical resistance initially increased, which is contrary to this prediction. This can be explained as follows: During the first week, irradiation-induced defects such as interstitial loops and vacancy clusters were generated in addition to the order-to-disorder phase change. These defects act as charge carrier scattering centers, increasing electrical resistance. Additionally, after some Ni atoms jump from B to D sites, those Ni atoms may be considered defects that can scatter charge carriers. This suppresses electron lifetime and in turn increases the electrical resistance. However, the Seebeck coefficient
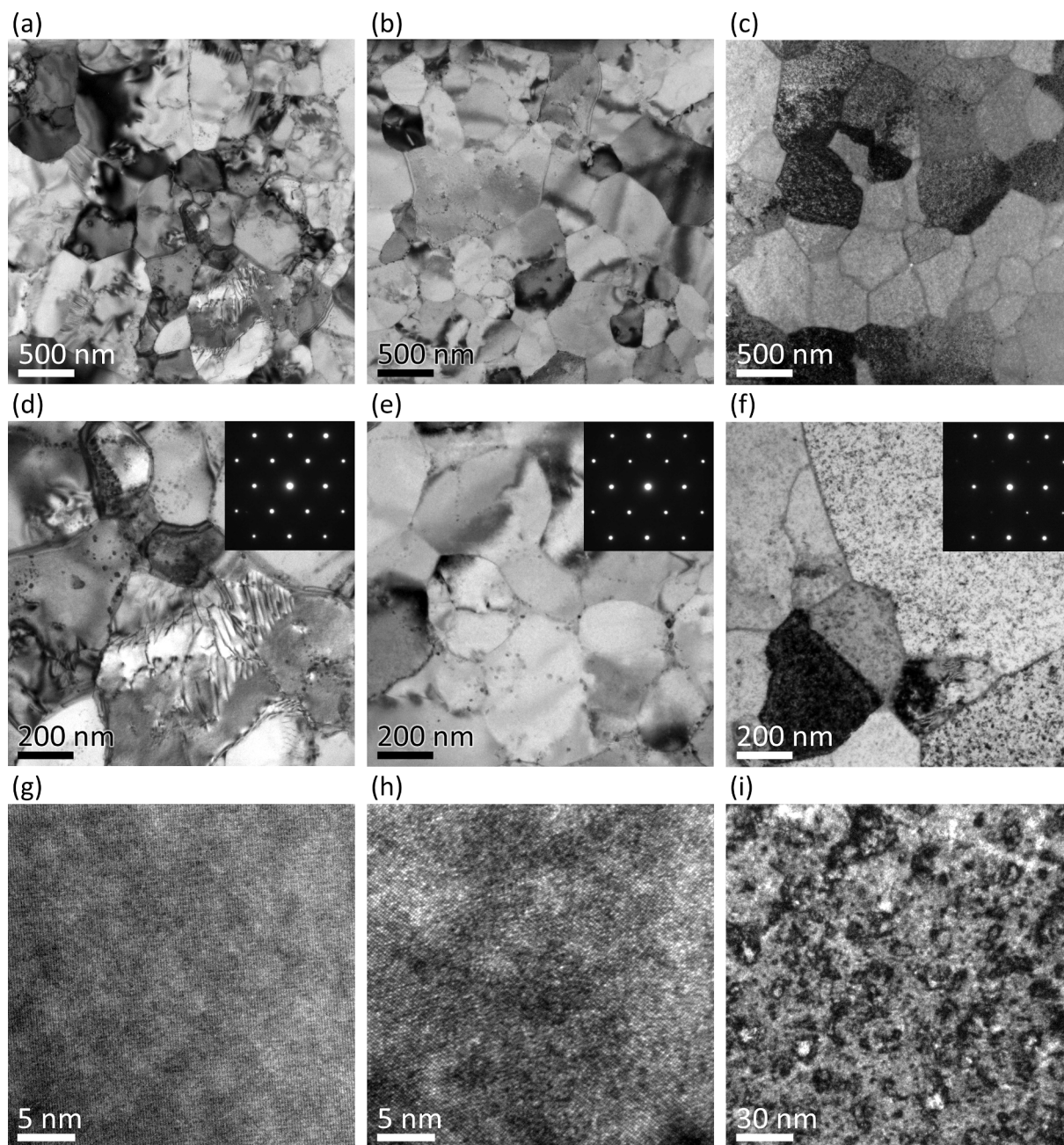
Fig. 4. Transmission Electron Microscopy of the n-type material: (a-i) Bright-field TEM of HHN (Hf$_{0.25}$Zr$_{0.75}$NiSn$_{0.99}$Sb$_{0.01}$) from the (a, d, g) non-irradiated region, (b, e) the region irradiated to 0.05 dpa, and (c, f, h, i) the region irradiated to 0.5 dpa with insets in (d-f) showing SAED patterns along the [1 1 0] zone axis. The center of each image corresponds to a depth of approximately 3 μm from the sample surface.

is less sensitive to electron lifetime so the Seebeck coefficient would be expected to decrease during the entirety of the first week at low temperature, which is indeed the case (Fig. 2b). In the case of electrical resistance, the scattering effect introduced by irradiation-induced defects outweighs the effect of the phase transition during the first half of the first week at low temperature when the electrical resistance is increasing; however, the phase transition effect becomes dominant as the change in electrical resistance levels off and subsequently begins to decrease on day 4 (Fig. 2b). The recovery from the chemically disordered phase to the original ordered phase after day 7 explains the initial sharp increase in TEG electrical resistance after the switch to high power on day 7. This is consistent with our model: When the temperature rises, the annealing effect drives Ni atoms back to B sites and the system becomes semiconducting again. The higher temperature also provides the

activation energy necessary for the ongoing annealing of irradiation induced defects, leading to the steadily decreasing TEG electrical resistance for the remainder of the time in the reactor.

This phase change mechanism is also consistent with the SAED patterns shown in Fig. 4. The electron diffraction pattern was simulated for A$_1$B$_{1-x}$C$_1$D$_x$, and the intensities of $\langle 2n-1, 2n-1, 2m-1 \rangle$ spots diminish as x increases (Supplementary Fig. S5). Comparing experimental and simulated SAED patterns, we obtain rough estimations of $x \sim 0.1$ under 0.05 dpa, and $x \sim 0.3$ under 0.5 dpa. The fact that x and dpa are close to each other supports the mechanism we proposed above. For example, if there are 0.5 displacements per atom, then (approximately) half of the Ni atoms have the chance to displace to the D sites, which would lead to $x \sim 0.5$.
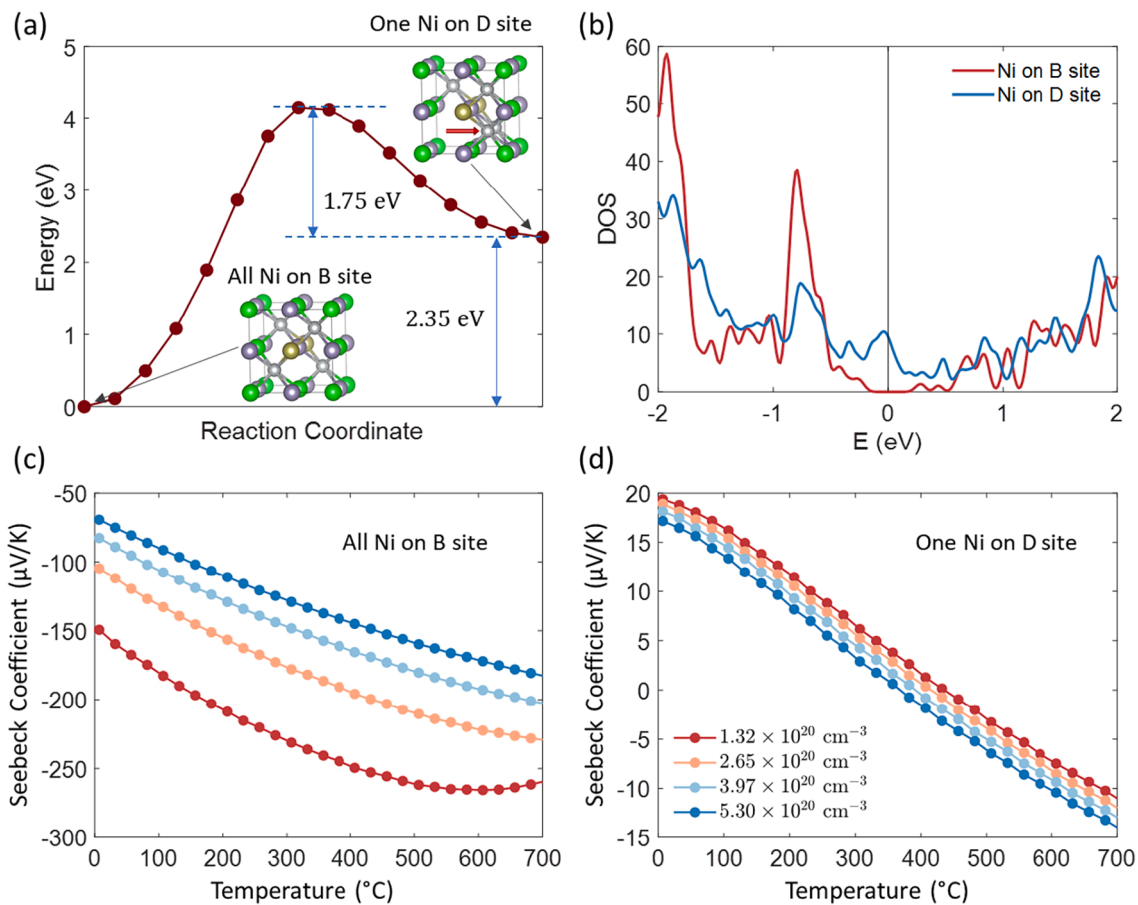
Fig. 5. Atomic phase change of $Hf_{0.25}Zr_{0.75}NiSn$: (a) the transition path for Ni to jump from B site to D site; (b) density of states when all Ni atoms are on B sites (red curve) and one of four Ni atoms is on D site (blue curve); (c, d) Seebeck coefficient with different carrier concentrations when all Ni atoms are on B sites (c) and one of four Ni atoms is on D site (d). For calculations in (b-d), a 12-atom $Hf_1Zr_3Ni_4Sn_4$ supercell is used.

5. Conclusions

A state-of-the-art nanostructured bulk TEG module was inserted into the core of the nuclear power reactor at MIT and the in-situ thermo-electric performance was monitored for 30 days. The reactor was brought to full power (5.7 MW) on the first day and the TEG quickly reached a peak power output of 1.5 W. The TEG temperatures were then decreased and held relatively low for the remainder of the first week, during which time the thermoelectric power output fell severely due to significantly diminished Seebeck voltage and increased electrical resistance. Immediately upon bringing the TEG to moderately high temperature on day 7, the power output increased by a factor of 20 due to a significant recovery in the Seebeck coefficients of the thermoelectric materials comprising the TEG. The TEG power output continued to increase for the remainder of the time in the reactor due to steadily increasing Seebeck voltage (continued recovery to the native chemically ordered phase) and decreasing electrical resistance (continued annealing of irradiation-induced defects that were introduced during the first week at low temperature).

The same materials comprising the TEG were selectively irradiated with alpha particles to uncover the effect of irradiation dose on material properties. Post irradiation examination revealed that defects (dislocation loops, vacancy clusters) were generated under irradiation. Such defects act as scattering sources for charge carriers, lowering mobility and increasing electrical resistance. A chemical order-to-disorder phase transition was also induced under irradiation. Specifically, the Ni (Fe) atoms jump to vacancy sites, rendering the HHN (HHP) system metallic. Simulations show that such a chemically disordered phase has

significantly lower Seebeck coefficient than the native phase, consistent with experimental results. When the TEG was brought to high temperature, thermal energy provided the kinetic facilitations necessary for the Ni (Fe) atoms to jump back to their original sites, restoring the semi-conducting nature of the thermoelectric materials comprising the TEG. The proposed phase transition mechanism and respective calculations are supported by SAED and SThM measurements.

This work provides new knowledge and understanding on the atomic/nanoscale origin of irradiation induced structure and property changes in nanostructured thermoelectric materials and is expected to expedite innovations and applications of nanostructured materials with enhanced radiation tolerance for nuclear energy applications. In particular, current high-ZT thermoelectric materials are clearly not optimized for in-radiation service, and there is a need for further materials explorations that would enable more advanced radiation-to-electrical energy conversions.

6. Methods

Thermoelectric generator fabrication. To construct the TEG device, n-type and p-type nanostructured bulk half-Heusler elements of sizes $1.8 \times 1.8 \times 2$ mm were brazed to copper electrodes at 825 °C in vacuum using a silver and copper-based brazing alloy (Incusil-ABA). The TEG module consists of 28n-type and p-type HH elements.

In-situ measurements. A current source and nanovoltmeter were used to measure the TEG electrical resistance, while a DC load and programmable multimeter were used to periodically perform current sweeps to measure the TEG power as a function of load resistance. Since

the hot- and cold-side temperatures of the TEG begin to change immediately upon pulling current, the peak power measured with the DC load was typically $\lesssim$ 4% of the peak power predicted by theory $P_{\max} = V_{\mathrm{oc}}^2/4R$, where V_{oc} is the open-circuit voltage of the TEG and R is the TEG electrical resistance. The TEG Seebeck voltage was monitored continuously with the programmable multimeter.

Scanning thermal microscopy. Microscale Seebeck coefficient and thermal conductivity were measured using a custom in-house fabricated SThM probe [36].

Modeling. The first-principles calculations are based on density functional theory (DFT) [38,39] as implemented in the Vienna *ab initio* simulation package (VASP) [40,41]. The exchange–correlation interactions are treated by a generalized gradient approximation (GGA) in the form of Perdew-Burke-Ernzerhof (PBE) [42]. Core and valence electrons are treated by projector augmented wave (PAW) method [43] and plane-wave basis functions, respectively. Then a tight-binding (TB) Hamiltonian is constructed from DFT results with the help of the Wannier90 package [44]. The TB Hamiltonian is utilized to calculate the Seebeck coefficients on a finer k-mesh. The k-mesh convergence for BZ integration is well tested.

CRediT authorship contribution statement

Nicholas Kempf: Conceptualization, Methodology, Software, Validation, Formal analysis, Investigation, Resources, Data curation, Writing – original draft, Writing – review & editing, Visualization, Supervision, Project administration. **Mortaza Saeidi-Javash:** Software, Formal analysis, Investigation. **Haowei Xu:** Methodology, Software, Validation, Formal analysis, Writing – review & editing, Visualization. **Sheng Cheng:** Investigation. **Megha Dubey:** Investigation. **Yaqiao Wu:** Investigation. **Joshua Daw:** Resources. **Ju Li:** Writing – review & editing, Supervision, Project administration, Funding acquisition. **Yanliang Zhang:** Conceptualization, Resources, Writing – review & editing, Supervision, Project administration, Funding acquisition.

Declaration of Competing Interest

The authors declare that they have no known competing financial interests or personal relationships that could have appeared to influence the work reported in this paper.

Data availability

Data will be made available on request.

Appendix A. Supplementary data

Supplementary data to this article can be found online at https://doi.org/10.1016/j.enconman.2022.115949.

References

[1] Marques JG. Evolution of nuclear fission reactors: Third generation and beyond. Energy Convers Manag 2010;51:1774–80.

[2] Lewis NS. A prospective on energy and environmental science. Energy Environ Sci 2019;12:16–8.

[3] Champier D. Thermoelectric generators: A review of applications. Energy Convers Manag 2017;140:167–81.

[4] Rowe DM. Thermoelectrics Handbook: Macro to Nano. CRC Press; 2005.

[5] Luo Z-Z, Cai S, Hao S, Bailey TP, Luo Y, Luo W, et al. Extraordinary role of Zn in enhancing thermoelectric performance of Ga-doped n-type PbTe. Energy Environ Sci 2022;15:368–75.

[6] He R, Zhu T, Wang Y, Wolff U, Jaud JC, Sotnikov A, et al. Unveiling the phonon scattering mechanisms in half-Heusler thermoelectric compounds. Energy Environ Sci 2020;13:5165–76.

[7] Zhu B, Liu X, Wang Q, Qiu Y, Shu Z, Guo Z, et al. Realizing record high performance in n-type Bi2Te3-based thermoelectric materials. Energy Environ Sci 2020;13:2106–14.

[8] You L, Zhang J, Pan S, Jiang Y, Wang K, Yang J, et al. Realization of higher thermoelectric performance by dynamic doping of copper in n-type PbTe. Energy Environ Sci 2019;12:3089–98.

[9] Xiao Y, Xu L, Hong T, Shi H, Wang S, Gao X, et al. Ultrahigh carrier mobility contributes to remarkably enhanced thermoelectric performance in n-type PbSe. Energy Environ Sci 2022;15:346–55.

[10] Hinterleitner B, Knapp I, Poneder M, Shi Y, Müller H, Eguchi G, et al. Thermoelectric performance of a metastable thin-film Heusler alloy. Nature 2019; 576:85–90.

[11] Iversen BB. Breaking thermoelectric performance limits. Nat Mater 2021;20: 1309–10.

[12] Zeier WG, Schmitt J, Hautier G, Aydemir U. Engineering half-Heusler thermoelectric materials using Zintl chemistry. Nat Rev Mater 2016. https://doi.org/10.1038/natrevmats.2016.32.

[13] Fu C, Bai S, Liu Y, Tang Y, Chen L, Zhao X, et al. Realizing high figure of merit in heavy-band p-type half-Heusler thermoelectric materials. Nat Commun 2015;6: 4–10.

[14] Clayton DA, Andrews WHJ & Lenarduzzi R. No Title. *ORNL, Rep. No. ORNL/TM-2012/442* 442 (2012).

[15] Wang H, Leonard KJ. Effect of high fluence neutron irradiation on transport properties of thermoelectrics. Appl Phys Lett 2017;111:1–5.

[16] Danko JC, Kilp GR, Mitchell PV. Irradiation effects on thermoelectric materials. Adv Energy Convers 1962. https://doi.org/10.1016/0365-1789(62)90011-5.

[17] Vandersande JW, McCormack J, Zoltan A, Farmer J. Effect of neutron irradiation on the thermoelectric properties of SiGe alloys. Proceedings of the Intersociety Energy Conversion Engineering Conference. 1990.

[18] Idnurm M, Landecker K. Changes produced in thermoelectric materials by thermal-neutron irradiation. Br J Appl Phys 1967. https://doi.org/10.1088/0508-3443/18/8/422.

[19] Li Y, Li J, Du J, Han J, Xiang Q, Zhang C. Influence of fast neutron and gamma irradiation on the thermoelectric properties of n-type and p-type SiGe alloy. J Nucl Mater 2020;528:151856.

[20] Chen S, Ren Z. Recent progress of half-Heusler for moderate temperature thermoelectric applications. Mater Today 2013;16:387–95.

[21] Chen S, Lukas KC, Liu W, Opeil CP, Chen G, Ren Z. Effect of Hf concentration on thermoelectric properties of nanostructured n-type half-heusler materials HfxZr1-xNiSn 0.99Sb0.01. Adv Energy Mater 2013;3:1210–4.

[22] He R, Kraemer D, Mao J, Zeng L, Jie Q, Lan Y, et al. Achieving high power factor and output power density in p-type half-Heuslers Nb1-xTixFeSb. Proc Natl Acad Sci U S A 2016;113:13576–81.

[23] Ren Q, Fu C, Qiu Q, Dai S, Liu Z, Masuda T, et al. Establishing the carrier scattering phase diagram for ZrNiSn-based half-Heusler thermoelectric materials. Nat Commun 2020;11:1–9.

[24] Shen Q, Chen L, Goto T, Hirai T, Yang J, Meisner GP, et al. Effects of partial substitution of Ni by Pd on the thermoelectric properties of ZrNiSn-based half-Heusler compounds. Appl Phys Lett 2001;79:4165–7.

[25] Xie H, Wang H, Pei Y, Fu C, Liu X, Snyder GJ, et al. Beneficial contribution of alloy disorder to electron and phonon transport in half-heusler thermoelectric materials. Adv Funct Mater 2013;23:5123–30.

[26] Yang J, Meisner GP, Chen L. Strain field fluctuation effects on lattice thermal conductivity of ZrNiSn-based half-Heusler compounds. Appl Phys Lett 2004;85: 1140–2.

[27] Liu Y, Xie H, Fu C, Snyder GJ, Zhao X, Zhu T. Demonstration of a phonon-glass electron-crystal strategy in (Hf, Zr)NiSn half-Heusler thermoelectric materials by alloying. J Mater Chem A 2015;3:22716–22.

[28] Sakurada S, Shutoh N. Effect of Ti substitution on the thermoelectric properties of (Zr, Hf)NiSn half-Heusler compounds. Appl Phys Lett 2005;86:1–3.

[29] Joshi G, Dahal T, Chen S, Wang H, Shiomi J, Chen G, et al. Enhancement of thermoelectric figure-of-merit at low temperatures by titanium substitution for hafnium in n-type half-Heuslers Hf0.75-xTixZr0.25NiSn0.99Sb0.01. Nano Energy 2013;2:82–7.

[30] Huang L, Zhang Q, Yuan B, Lai X, Yan X, Ren Z. Recent progress in half-Heusler thermoelectric materials. Mater Res Bull 2016;76:107–12.

[31] Joshi G, Yan X, Wang H, Liu W, Chen G, Ren Z. Enhancement in thermoelectric figure-of-merit of an N-type half-Heusler compound by the nanocomposite approach. Adv Energy Mater 2011;1:643–7.

[32] Bhardwaj A, Misra DK, Pulikkotil JJ, Auluck S, Dhar A, Budhani RC. Implications of nanostructuring on the thermoelectric properties in half-Heusler alloys. Appl Phys Lett 2012;101.

[33] Zhang Y, Cleary M, Wang X, Kempf N, Schoensee L, Yang J, et al. High-temperature and high-power-density nanostructured thermoelectric generator for automotive

waste heat recovery. Energy Convers Manag 2015. https://doi.org/10.1016/j.enconman.2015.08.051.

[34] Kempf N, Zhang Y. Design and optimization of automotive thermoelectric generators for maximum fuel efficiency improvement. Energy Convers Manag 2016. https://doi.org/10.1016/j.enconman.2016.05.035.

[35] Zhang Y, Wang X, Cleary M, Schoensee L, Kempf N, Richardson J. High-performance nanostructured thermoelectric generators for micro combined heat and power systems. Appl Therm Eng 2016. https://doi.org/10.1016/j.applthermaleng.2015.11.064.

[36] Kempf N, Zhang Y. A robust high sensitivity scanning thermal probe for simultaneous microscale thermal and thermoelectric property mapping. Appl Phys Lett 2021;119:1ENG.

[37] Henkelman G, Uberuaga BP, Jónsson H. Climbing image nudged elastic band method for finding saddle points and minimum energy paths. J Chem Phys 2000;113:9901–4.

[38] Hohenberg P, Kohn W. Inhomogeneous Electron Gas. Phys Rev 1964;136:B864–71.

[39] Kohn W, Sham LJ. Self-Consistent Equations Including Exchange and Correlation Effects. Phys Rev 1965;140:A1133–1138s.

[40] Kresse G, Furthmüller J. Efficiency of ab-initio total energy calculations for metals and semiconductors using a plane-wave basis set. Comput Mater Sci 1996;6:15–50.

[41] Kresse G, Furthmüller J. Efficient iterative schemes for ab initio total-energy calculations using a plane-wave basis set. Phys Rev B 1996;54:11169–86.

[42] Perdew JP, Burke K, Ernzerhof M. Generalized gradient approximation made simple. Phys Rev Lett 1996;77:3865–8.

[43] Blöchl PE. Projector augmented-wave method. Phys Rev B 1994;50:17953–79.

[44] Mostofi AA, Yates JR, Pizzi G, Lee YS, Souza I, Vanderbilt D, et al. An updated version of wannier90: A tool for obtaining maximally-localised Wannier functions. Comput Phys Commun 2014;185:2309–10.

1 # Electronic Supplementary Information

2 ## Thermoelectric Power Generation in the Core of a Nuclear Reactor†

3 Nicholas Kempf,[a‡] Mortaza Saeidi-Javash,[a‡] Haowei Xu,[b‡] Sheng Cheng,[cd] Megha Dubey,[cd] Yaqiao

4 Wu,[cd] Joshua Daw,[e] Ju Li[b,**] and Yanliang Zhang[a,*,**]

5

6 [a]Department of Aerospace and Mechanical Engineering, University of Notre Dame, Notre Dame, IN 46556,

7 USA

8 [b]Department of Nuclear Science and Engineering, Massachusetts Institute of Technology, Cambridge, MA

9 02139, USA

10 [c]Micron School of Materials Science and Engineering, Boise State University, Boise, ID 83725 USA

11 [d]Microscopy and Characterization Suite, Center for Advanced Energy Studies, Idaho Falls, ID 83401 USA

12 [e]Measurement Sciences Laboratory, Idaho National Laboratory, Idaho Falls, ID 83415, USA

13 *Email: yzhang45@nd.edu

14 †Electronic supplementary information (ESI) available. See [to be determined]

15 ‡,**These authors contributed equally to this work

16
17 ## Test capsule

18 A model of the test capsule that contained the TEG and tungsten susceptor inside the nuclear

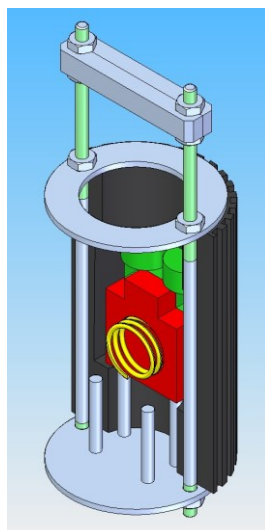19 reactor is shown in Fig. S1.

20

21
22 **Fig. S1.** Solidworks half-model of the test capsule showing the graphite shell (black), titanium support beams

23 (silver/gray and light green), susceptor (red), and spring (yellow). The TEG is mostly hidden by the heater, shown

24 in dark green.

1

25   The test capsule shown in Fig. S1 contains a primary graphite shell that houses the TEG,

26   susceptors, thermocouples, and a spring. Graphite was chosen due to its low neutron-activation

27   cross-section as well as its low thermal excitation by gamma rays. The graphite shell is held

28   together partially by the titanium rods shown in Fig. S1 and partially by a metal tube through

29   which the entire test capsule is fed (not shown in Fig. S1).

30   The partially assembled test capsule shown in **Fig. S2** serves several purposes. First, it

31   applies pressure between the susceptor and the hot side of the TEG as well as between the cold

32   side of the TEG and the graphite shell of the test capsule. The grooves seen running along the

33   length of the test capsule are where a cooling gas (a mixture of Helium and Neon) flows to

34   provide the cold side and thus the temperature difference across the TEG. Finally, the metal

35   fixtures seen on the top of the capsule provide an anchor point to eliminate any mechanical

36   stress on the electrical wires that connect to the TEG.
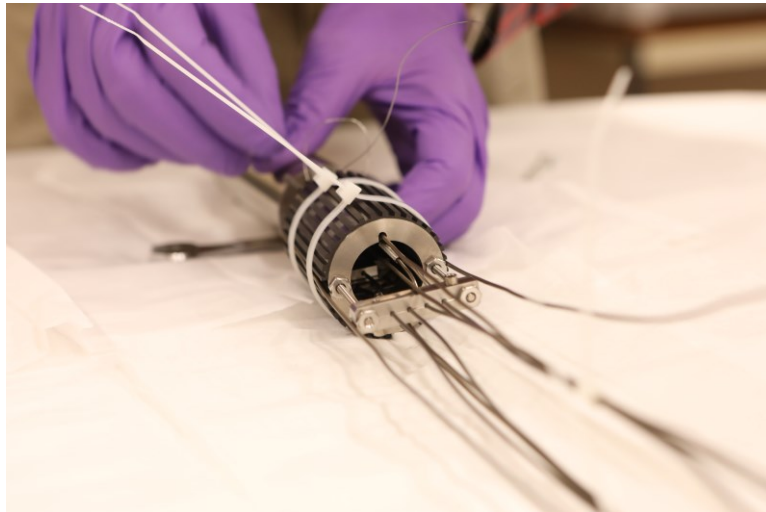
37
38   **Fig. S2.** Photograph of the partially assembled graphite and titanium test capsule. The plastic zip-ties are

39   temporary and are cut off before the test capsule is fed into the tube that is placed in the reactor core.

40   Not completely visible in **Fig. S2** is a tungsten susceptor which provides 75 W of heating power,

41   generating the temperature gradient across the TEG.

2

Thermoelectric generator in-core performance measurement

The voltage of the TEG was continuously monitored with an Agilent 34970A data acquisition/switch unit. The TEG electrical resistance R_{TEG} was measured approximately every 2 to 4 minutes with a Keithley 6221 current source and a Keithley 2182A nanovoltmeter. Delta resistance measurements were performed to eliminate the influence of thermoelectric voltages on the resistance measurement. The TEG power output as a function of load resistance was measured approximately every 2 to 4 minutes by varying the load resistance with a B&K Precision 8500 DC load while the voltage was measured using the Agilent 34970A during the current sweep. Each current sweep consisted of approximately 10 current steps and the time at each current was minimized. The TEG hot- and cold-side temperatures were allowed to restabilize before the subsequent electrical resistance and power measurement.

Ion irradiation and scanning thermal microscopy

Shown in **Fig. S3** are the n- and p-type bars prepared for ion irradiation with copper shields suspended over selected regions of the bars.


Fig. S3. Thermoelectric bars prepared for ion irradiation. Photograph of the two polished half-Heusler bars prepared for irradiation with copper bridges suspended above selected regions of the bars.

After irradiation, the copper shields were removed and microscale Seebeck coefficient and thermal conductivity were measured using a novel surface-sensitive scanning thermal microprobe described elsewhere [1]. The SThM probe was scanned back and forth along the length of the bar with 200 μm spacing between measurement locations.

3

Transmission electron microscopy and electron diffraction of the p-type material

The TEM with SAED of the ion irradiated HHP material is shown in **Fig. S4**.
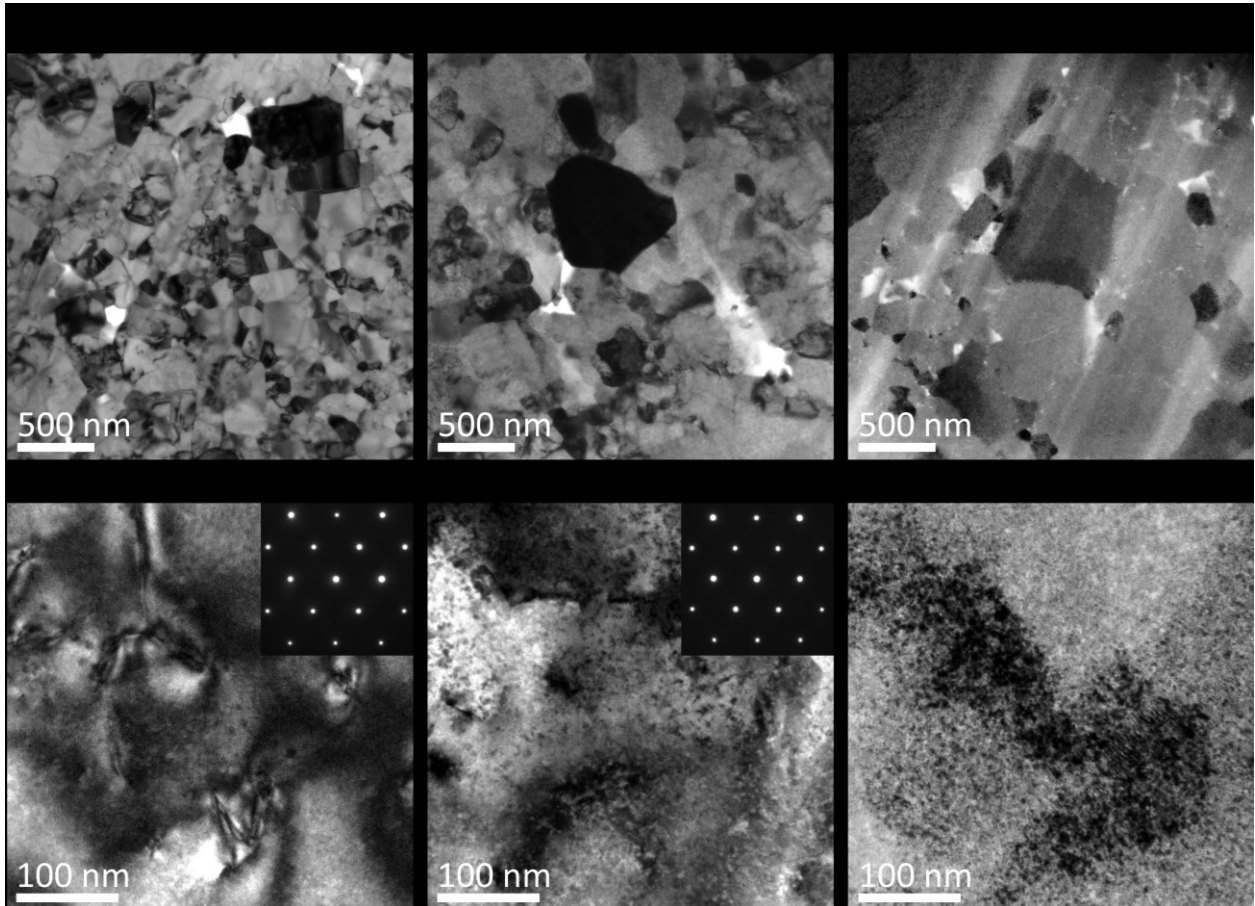
Fig. S4. Transmission Electron Microscopy of the p-type material: (a-f) Bright-field TEM of HHP ($Nb_{0.75}Ti_{0.25}FeSb$) from the (a, d) non-irradiated region, (b, e) the region irradiated to 0.05 dpa, and (c, f) the region irradiated to 0.5 dpa with insets in (d-f) showing SAED patterns along the [110] zone axis. The center of each image corresponds to a depth of approximately 3 µm from the sample surface.

## Atomic-level modeling

The simulated SAED patterns of HHN in **Fig. S5** show that with increasing level of chemical disorder, there is decreasing spot intensity for the family of planes of the form $\langle 2n-1, 2n-1, 2m-1 \rangle$, where $n, m = 1, 2, \ldots$.

4

78   **Fig. S5.** Simulated SAED patterns of the n-type half-Heusler material for various irradiation doses. a-c, Simulated

79   SEAD pattern of $Hf_{0.25}Zr_{0.75}NiSn$ with $AB_{1-x}CD_x$ occupations: $x=0$ (a), $x=0.25$ (b), and $x=0.5$ (c).

80   The results of the ab initio calculations for the p-type material (HHP) are shown in **Fig. S6**.
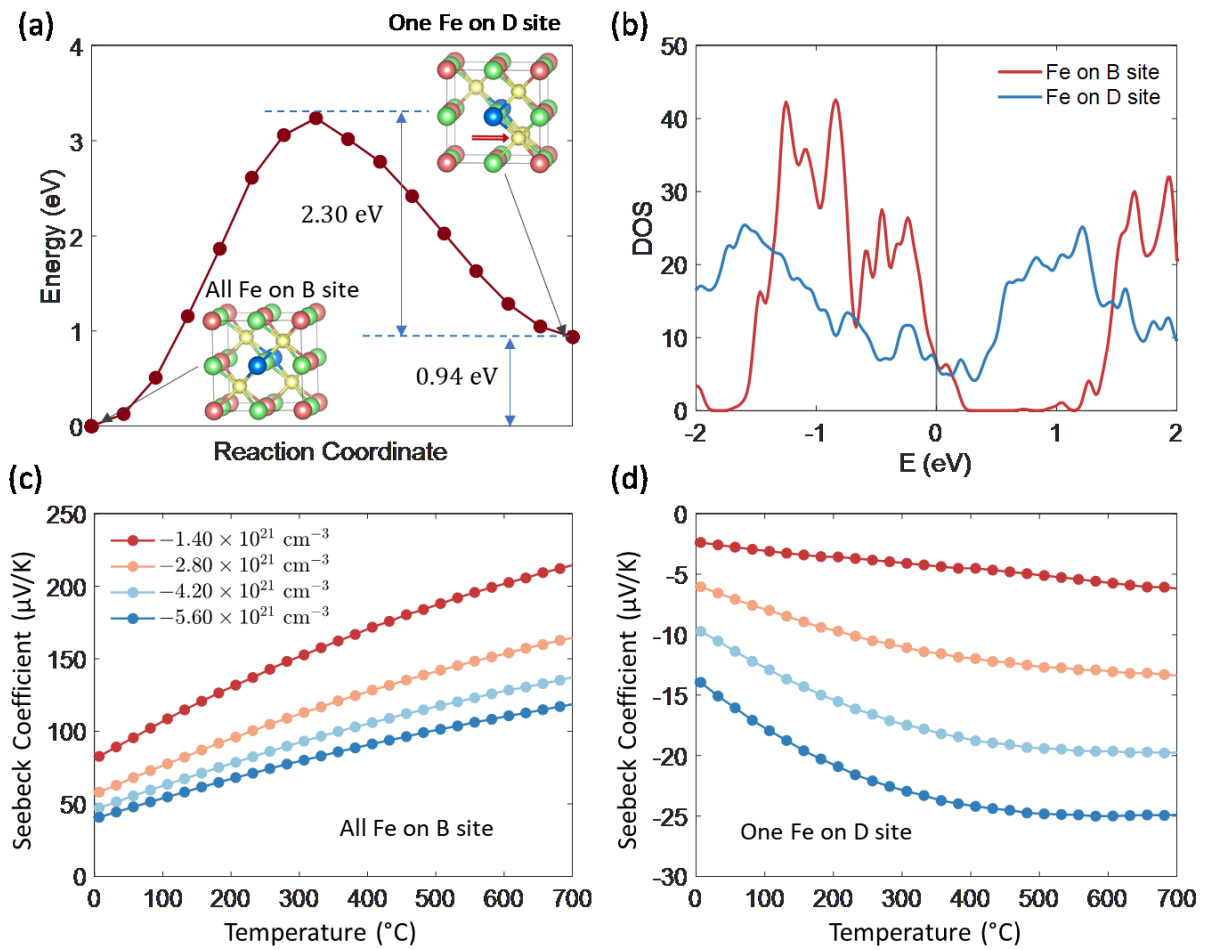
81
82   **Fig. S6.** Atomic phase change of $Nb_{0.75}Ti_{0.25}FeSb$: (a) The transition path for Fe to jump from B site to D site; (b)

83   Density of states when all Fe atoms are on B sites (red curve) and one of four Ni atoms is on D site (blue curve); (c,

84   d) Seebeck coefficient with different carrier concentrations when all Fe atoms are on B sites (c) and one of four Fe

85   atoms is on D site (d). For calculations in b-d, a 12-atom $Nb_3Ti_1Fe_4Sb_4$ supercell is used.

86

References

1. Kempf N & Zhang Y. A robust high sensitivity scanning thermal probe for simultaneous microscale thermal and thermoelectric property mapping. *Appl. Phys. Lett.* 119, 1ENG (2021).

6